

# Molecular/electronic structure–surface acidity relationships of model-supported tungsten oxide catalysts

Taejin Kim<sup>a</sup>, Andrew Burrows<sup>b</sup>, Christopher J. Kiely<sup>b</sup>, Israel E. Wachs<sup>a,\*</sup>

<sup>a</sup> *Operando Molecular Spectroscopy & Catalysis Laboratory, Chemical Engineering Department, Lehigh University, Bethlehem, PA 18015, USA*

<sup>b</sup> *Center for Advanced Materials and Nanotechnology, Materials Science & Engineering Department, Lehigh University, Bethlehem, PA 18015, USA*

Received 30 August 2006; revised 20 October 2006; accepted 30 December 2006

Available online 1 February 2007

## Abstract

A series of model-supported  $\text{WO}_3$  catalysts were synthesized on preformed  $\text{Al}_2\text{O}_3$ ,  $\text{Nb}_2\text{O}_5$ ,  $\text{TiO}_2$ , and  $\text{ZrO}_2$  supports by impregnation of aqueous ammonium metatungstate,  $(\text{NH}_4)_{10}\text{W}_{12}\text{O}_{41}\cdot 5\text{H}_2\text{O}$ . The molecular and electronic structures of the supported tungsten oxide phases were determined with in situ Raman and UV–vis spectroscopy, respectively. The supported tungsten oxide structures are the same on all oxide supports as a function of tungsten oxide surface density ( $\text{W}/\text{nm}^2$ ). Below monolayer coverage ( $<5 \text{ W}/\text{nm}^2$ ), both monotungstate and polytungstate surface  $\text{WO}_x$  species are present under dehydrated conditions and the polytungstate/monotungstate ratio increases with increasing surface coverage. Above monolayer coverage ( $>5 \text{ W}/\text{nm}^2$ ), crystalline  $\text{WO}_3$  nanoparticles are present on top of the surface  $\text{WO}_x$  monolayer. Above  $\sim 10 \text{ W}/\text{nm}^2$ , bulk-like  $\text{WO}_3$  crystallites become dominant. The number of catalytic active sites and surface chemistry of the supported tungsten oxide phases were chemically probed with  $\text{CH}_3\text{OH}$  dehydration to  $\text{CH}_3\text{OCH}_3$ . The specific oxide support was found to significantly affect the relative catalytic acidity of the surface  $\text{WO}_x$  species ( $\text{Al}_2\text{O}_3 \gg \text{TiO}_2 > \text{Nb}_2\text{O}_5 > \text{ZrO}_2$ ) to that of the supported  $\text{WO}_3$  nanoparticles. Consequently, no general relationship exists between the molecular/electronic structures or domain size and the specific catalytic acidity of the supported tungsten oxide phases present in the model-supported  $\text{WO}_3$  catalysts.

© 2007 Elsevier Inc. All rights reserved.

**Keywords:** Spectroscopy; Raman; UV–vis; TPSR; HR-TEM; Catalysts; Supported;  $\text{WO}_3$ ;  $\text{Al}_2\text{O}_3$ ;  $\text{ZrO}_2$ ;  $\text{TiO}_2$ ;  $\text{Nb}_2\text{O}_5$ ;  $\text{CH}_3\text{OH}$ ;  $\text{CH}_3\text{OCH}_3$ ; Dehydration

## 1. Introduction

Supported tungsten oxide catalysts are used in many significant industrial applications and are known to be efficient solid acid catalysts [1,2]. Tungsten oxide on alumina catalysts are used for hydrotreating and for hydrocarbon cracking reactions [3–7], and also exhibit enhanced resistance to reduction [8]. Tungsten oxide supported on titania, in combination with vanadia, is effective for both the selective catalytic reduction of NO by  $\text{NH}_3$  to  $\text{N}_2/\text{H}_2\text{O}$  and for alkene isomerization [9,10]. As an alternative to the sulfated zirconia solid acid catalyst, supported  $\text{WO}_3/\text{ZrO}_2$  catalysts also have been reported to be active for the isomerization of  $\text{C}_4$ – $\text{C}_8$  alkanes [11–13]. In contrast to the above supported tungsten oxide catalytic systems,

the supported  $\text{WO}_3/\text{Nb}_2\text{O}_5$  catalysts have not received as much attention [14–16].

In many cases, the interaction of a catalytic active component, such as tungsten oxide, with an oxide support ( $\text{Al}_2\text{O}_3$ ,  $\text{ZrO}_2$ ,  $\text{TiO}_2$ , and  $\text{Nb}_2\text{O}_5$ ) can dramatically alter the structural and catalytic properties of supported catalytic active component [17]. For most such strongly interacting oxide systems, the supported catalytic active metal oxide phase is molecularly dispersed as a two-dimensional metal oxide overlayer on a high surface area support oxide [17]. The nature of the surface tungsten oxide phases on oxide supports have been characterized with many different techniques to provide insights into their molecular and electronic structures as well as provide information their corresponding surface chemical properties [17–27]. In spite of the large body of literature on this subject, the molecular/electronic structure–catalytic activity relationships of supported tungsten oxide catalysts are still not satisfactorily understood. Consequently, the objective of this paper is to investigate

\* Corresponding author. Fax: +1 610 758 6555.  
E-mail address: [iew0@lehigh.edu](mailto:iew0@lehigh.edu) (I.E. Wachs).

the molecular/electronic and the surface reactivity properties of model-supported tungsten oxide catalysts and to establish the relationships between these parameters. In the present study both the surface tungsten oxide coverage ( $\text{W}/\text{nm}^2$ ) and the specific oxide support, preformed model supports, were varied over a wide range to carefully examine the influence of these two significant parameters. The tungsten oxide molecular structures were determined with in situ Raman spectroscopy and the corresponding electronic structures were determined with in situ UV–vis diffuse reflectance spectroscopy (DRS). The acidic nature of the supported tungsten oxide phases were chemically probed with temperature programmed surface reaction (TPSR) spectroscopy and steady-state dehydration of methanol to dimethyl ether ( $\text{CH}_3\text{OCH}_3$ ).

## 2. Experimental

### 2.1. Catalyst synthesis

The supported tungsten oxide catalysts were all prepared by incipient wetness impregnation of aqueous ammonium metatungstate,  $(\text{NH}_4)_{10}\text{W}_{12}\text{O}_{41}\cdot 5\text{H}_2\text{O}$  (Pfaltz & Bauer, 99.5% purity), onto different oxide supports:  $\text{Al}_2\text{O}_3$  (Harshaw/Engelhard,  $178 \text{ m}^2/\text{g}$ ),  $\text{TiO}_2$  (Degussa P-25,  $51 \text{ m}^2/\text{g}$ ),  $\text{Nb}_2\text{O}_5$  (CBMM AD1927 HY-340,  $66 \text{ m}^2/\text{g}$ ), and  $\text{ZrO}_2$  (Degussa,  $60 \text{ m}^2/\text{g}$ ). After impregnation, the samples were initially dried at room temperature overnight and then calcined in flowing air for 4 h at  $450^\circ\text{C}$ . Several supported  $\text{WO}_3/\text{ZrO}_2$  catalysts were also calcined at elevated temperatures ( $700$ – $900^\circ\text{C}$ ) to examine the effect of calcination temperature.

### 2.2. BET specific surface area measurement

The BET surface areas of the samples were measured by nitrogen adsorption–desorption in flowing  $\text{N}_2$  at  $-196^\circ\text{C}$  with a Quantasorb surface area analyzer (Quantachrome Corporation, Model OS-9). A sample quantity of  $\sim 0.3 \text{ g}$  was used for the measurement, and the sample was outgassed at  $250^\circ\text{C}$  before  $\text{N}_2$  adsorption (Quantachrome Corporation, Model QT-3).

### 2.3. Raman spectroscopy

The Raman spectra of the dehydrated supported tungsten oxide catalysts were obtained with either visible ( $532 \text{ nm}$ ) or UV ( $325 \text{ nm}$ ) excitation (Horiba-Jobin Yvon LabRam-HR). The UV laser excitation was generated from a He–Cd laser (Kimmon, Model IK5751 I-G,  $30 \text{ mW}$ ) and the visible excitation was generated by a Yag double-diode pumped laser (coherent  $315 \text{ m}$ ,  $20 \text{ mW}$ ). The scattered photons were directed into a single monochromator and focused onto a  $\text{LN}_2$  cooled CCD detector (JY-CCD3000V). The Raman spectrometer was equipped with an in situ environmental cell (Linkam T1500 cell) where both the temperature and the gaseous composition were controllable. The catalysts were maintained in loose powder form, initially dehydrated at  $450^\circ\text{C}$  for 1 h in flowing 10%  $\text{O}_2/\text{He}$  (Airgas, ultra-high purity and hydrocarbon-free), and the Raman spectra of the dehydrated samples were collected after

cooling the catalysts back to room temperature in the flowing 10%  $\text{O}_2/\text{He}$  gas. The spectral acquisition time used was 30 scans of 30 s/scan for a total of 15 min/spectrum.

### 2.4. UV–vis diffuse reflectance spectroscopy (DRS)

The UV–vis spectra of the dehydrated supported tungsten oxide catalysts were measured with a Varian Cary 5E UV–vis–NIR spectrophotometer. The catalysts in powder form were loaded into an environmental cell (Harrick, HVC-DR2) for obtaining their UV–vis spectra. The UV–vis spectra of the dehydrated samples were obtained at room temperature after calcination at  $400^\circ\text{C}$  in flowing 10%  $\text{O}_2/\text{He}$  gas for 1 h and cooling back to room temperature. A magnesium oxide sample was used as the standard for obtaining the baseline. Microsoft Excel software was used to calculate the Kubelka–Munk function  $F(R_\infty)$  and the edge energy ( $E_g$ ) from the absorbance data. Below  $300 \text{ nm}$ , the absorbance signal was unacceptably noisy and a filter (Varian, 1.5 ABS) was used to minimize the background noise. The UV–vis spectra were only collected for the supported  $\text{WO}_3/\text{ZrO}_2$  and  $\text{WO}_3/\text{Al}_2\text{O}_3$  catalysts because the strong oxide absorbance by the  $\text{TiO}_2$  and  $\text{Nb}_2\text{O}_5$  supports in the region of interest prevented collection of their supported tungsten oxide UV–vis spectra. The  $\text{Al}_2\text{O}_3$  support possesses no absorbance and the  $\text{ZrO}_2$  support exhibits very weak absorbance in the region of interest. The supported  $\text{WO}_3/\text{ZrO}_2$  UV–vis spectra were background subtracted with the  $\text{ZrO}_2$  support spectrum to account for zirconia's weak contribution to the UV–vis spectrum. In addition, the  $E_g$  values for the 2D surface  $\text{WO}_x$  and the 3D  $\text{WO}_3$  phases were independently determined by background subtracting the 2D surface  $\text{WO}_x$  monolayer UV–vis DRS contribution when monolayer surface coverage was exceeded.

### 2.5. High resolution-transmission electron microscopy (HR-TEM)

Samples for HR-TEM examination were prepared by dispersing the catalyst powder in high purity ethanol, then allowing a drop of the suspension to evaporate on a holey carbon film supported by a 300 mesh copper TEM grid. HR-TEM images of the ambient samples were obtained using a JEOL 2200FS transmission electron microscope, having an accelerating voltage of  $200 \text{ kV}$ , a point-to-point resolution of  $0.19 \text{ nm}$  and an information limit of  $0.11 \text{ nm}$ . Fourier transform (FT) analyses of lattices fringe periodicities and inter-planar angles were carried out using digital micrograph.

### 2.6. $\text{CH}_3\text{OH}$ temperature-programmed surface reaction (TPSR) spectroscopy

Methanol TPSR spectroscopy was performed on an Altamira temperature programmed system (AMI-200) equipped with an online quadrupole mass spectrometer (Dycor Dymaxion DME200MS). Samples of  $\sim 100 \text{ mg}$  were loaded into a U-shaped quartz tube and initially calcined at  $400^\circ\text{C}$  (Airgas,

ultra zero grade air, 30 ml/min) for 40 min to remove any possible adsorbed organic impurities and to dehydrate the catalysts. To ensure that the supported tungsten oxide species on the catalysts remain in a fully oxidized state, the pretreated samples were first cooled down in flowing air to 110 °C and then the gas stream was switched to an ultra high purity He (Airgas) flow on further cooling to 100 °C. After flushing with flowing He for another 30 min at 100 °C to remove any physically adsorbed oxygen and possible background gases, a CH<sub>3</sub>OH/He gas mixture feed (30 ml/min) containing 2000 ppm methanol was introduced for chemisorption for 30 min. Previous work demonstrated that methanol adsorption at 100 °C minimizes the formation of physically adsorbed methanol on the samples because physically adsorbed CH<sub>3</sub>OH desorbs below this temperature from oxide surfaces [28,29]. After methanol adsorption, the samples were again purged at 100 °C with flowing He for an additional hour to remove any residual physically adsorbed methanol. The CH<sub>3</sub>OH-TPSR experiments were performed with a heating rate of 10 °C/min in flowing UHP He and the desorbing molecules were monitored with the on-line MS. The *m/e* values used to detect the different desorption products were CH<sub>3</sub>OH (*m/e* = 31), H<sub>2</sub>CO (*m/e* = 30), CH<sub>3</sub>OCH<sub>3</sub> (DME; *m/e* = 45), (CH<sub>3</sub>O)<sub>2</sub>CH<sub>2</sub> (DMM; *m/e* = 75), H<sub>2</sub>O (*m/e* = 18), CO<sub>2</sub> (*m/e* = 44), and CO (*m/e* = 28). For those desorbing molecules that gave rise to several fragments in the mass spectrometer, additional *m/e* values were also collected to further confirm their identity. The activation energy for formation of dimethyl ether was calculated using the Redhead equation for first-order kinetics [30]. Previous studies demonstrated that the rate-determining step in methanol dehydration involves the first-order process that breaks the C–O bond in the surface CH<sub>3</sub>O\* intermediate [31]. In addition, the area under the DME/CH<sub>3</sub>OH-TPSR curve corresponds to the number of exposed surface acid sites.

### 2.7. Steady-state dehydration of methanol to dimethyl ether

Methanol dehydration was used to chemically probe the catalytic activity and product selectivity of the supported tungsten oxide catalysts. The dehydration of methanol was examined in a fixed-bed reactor at 230 °C with 30 mg of catalyst. The catalysts were suspended between two layers of quartz wool in a vertical glass tube. The volume composition of the gaseous reactant feed was CH<sub>3</sub>OH/O<sub>2</sub>/He = 6/13/81 (mol%) with a total flow rate of 100 ml/min from the top to the bottom of the reactor. The outlet of the reactor to the gas chromatograph was heated at ~130 °C in order to avoid product condensation. On-line analysis of the methanol conversions and reaction products was performed with an HP-5840A gas chromatograph containing two packed columns (Porapak R and Carbosieve SII) and two detectors (TCD and FID). Blank runs without the catalysts demonstrated negligible methanol conversion in the reactor system. The supported tungsten oxide catalysts were pretreated at 350 °C for 30 min in a stream of O<sub>2</sub>/He before each run. The catalytic experiments were run for 4 h at 230 °C to obtain the methanol conversion, selectivity, and activity. The steady-state methanol dehydration catalytic data were expressed in terms of

turnover frequency (TOF: number of DME molecules/surface acid site/s). For the supported tungsten oxide catalysts below monolayer surface coverage, the number of surface acid sites was taken as the number of surface WO<sub>x</sub> species, which assumed 100% dispersion and was independently confirmed with Raman spectroscopy. Above monolayer surface tungsten oxide coverage, the number of exposed surface acid sites was determined by the area under the DME/CH<sub>3</sub>OH-TPSR curves and normalized to the value for monolayer coverage.

## 3. Results

### 3.1. BET specific surface area and tungsten oxide surface density

The BET surface area and tungsten oxide surface density (W/nm<sup>2</sup>) for the supported tungsten oxide catalysts were determined and are listed in Table 1. The BET surface area continuously decreases with increasing tungsten oxide loading due to the additional mass introduced by the supported tungsten oxide phase. The tungsten oxide surface density (W/nm<sup>2</sup>) was calculated by using the initial BET surface area of the oxide supports because the supports retain their initial BET values for this rather mild calcination temperature and in the presence of surface tungsten oxide species that are known to retard sintering of oxide support.

### 3.2. In situ Raman spectroscopy

#### 3.2.1. Supported WO<sub>3</sub>/Al<sub>2</sub>O<sub>3</sub> catalysts

The UV Raman spectra of the dehydrated WO<sub>3</sub>/Al<sub>2</sub>O<sub>3</sub> samples as a function of surface tungsten oxide density are presented in Fig. 1. The UV excitation was used because of sample fluorescence when excited in the visible region [32]. At low surface tungsten oxide density (0.5–4 W/nm<sup>2</sup>), only the Raman band characteristic of dehydrated surface WO<sub>x</sub> species is present. The surface nature of these dehydrated tungsten oxide species is confirmed by their reversible structural transformations on hydration–dehydration treatments (not shown for brevity). The Raman band in the 1003–1015 cm<sup>-1</sup> region arises

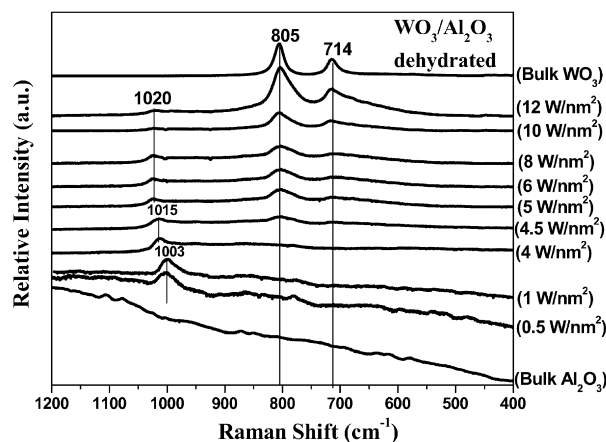


Fig. 1. UV Raman spectra of the model-supported WO<sub>3</sub>/Al<sub>2</sub>O<sub>3</sub> catalysts under dehydrated conditions.

Table 1  
BET surface area and tungsten oxide surface density ( $\text{W}/\text{nm}^2$ ) of the supported  $\text{WO}_3$  catalysts on the model oxide supports ( $\text{TiO}_2$ ,  $\text{Nb}_2\text{O}_5$ ,  $\text{Al}_2\text{O}_3$ , and  $\text{ZrO}_2$ )

Sample (calcination temperature, °C)	Surface density ( $\text{W}/\text{nm}^2$ )	BET surface area ( $\text{m}^2/\text{g}$ )
<b>Bulk <math>\text{TiO}_2</math></b>	0.0	51.0
5.0 wt% WTi (450)	2.7	48.1
7.3 wt% WTi (450)	4.0	46.4
8.1 wt% WTi (450)	4.5	46.1
13.6 wt% WTi (450)	8.0	43.0
16.4 wt% WTi (450)	10.0	41.4
19.1 wt% WTi (450)	12.0	39.3
<b>Bulk <math>\text{Nb}_2\text{O}_5</math></b>	0.0	66.0
3.2 wt% WNb (450)	1.3	64.0
9.2 wt% WNb (450)	4.0	56.7
10.2 wt% WNb (450)	4.5	55.8
16.9 wt% WNb (450)	8.0	51.3
20.3 wt% WNb (450)	10.0	47.8
23.4 wt% WNb (450)	12.0	43.6
<b>Bulk <math>\text{Al}_2\text{O}_3</math></b>	0.0	178.0
3.2 wt% WAl (450)	0.5	166.2
6.4 wt% WAl (450)	1.0	166.0
21.5 wt% WAl (450)	4.0	158.8
23.5 wt% WAl (450)	4.5	145.6
25.6 wt% WAl (450)	5.0	133.0
29.1 wt% WAl (450)	6.0	126.0
35.4 wt% WAl (450)	8.0	125.3
40.7 wt% WAl (450)	10.0	108.2
45.1 wt% WAl (450)	12.0	96.9
57.8 wt% WAl (450)	20.0	75.0
<b>Bulk <math>\text{ZrO}_2</math></b>	0.0	60.0
1 wt% WZr (450)	0.4	59.9
4 wt% WZr (450)	1.8	59.6
5 wt% WZr (450)	2.3	59.4
6 wt% WZr (450)	2.8	59.3
7 wt% WZr (450)	3.3	59.3
8.3 wt% WZr (450)	3.9	58.7
9.4 wt% WZr (450)	4.5	55.6
10 wt% WZr (450)	4.8	55.3
12 wt% WZr (450)	5.9	54.5
15 wt% WZr (450)	7.6	49.0
20 wt% WZr (450)	10.8	45.3
21.7 wt% WZr (450)	12.0	45.1
25.0 wt% WZr (450)	14.4	45.0
40.0 wt% WZr (450)	28.9	32.8

from the symmetric stretching vibrations of the terminal  $\text{W}=\text{O}$  bonds of surface  $\text{WO}_x$  species [15,33]. The shift of the surface  $\text{W}=\text{O}$  band with increasing tungsten oxide surface density is related to the polymerization of the surface  $\text{WO}_x$  species from monotungstate to polytungstate species [15]. No Raman bands due to crystalline  $\text{WO}_3$  particles at  $\sim 805$  and  $\sim 714$   $\text{cm}^{-1}$  are present for samples with less than  $5$   $\text{W}/\text{nm}^2$  [34]. At tungsten oxide surface densities of  $5$   $\text{W}/\text{nm}^2$  and above, Raman bands of crystalline  $\text{WO}_3$  also appear at  $\sim 805$  and  $\sim 714$   $\text{cm}^{-1}$  (see Fig. 1 for the bulk crystalline  $\text{WO}_3$  Raman spectrum). Note the Raman bands for the alumina-supported  $\text{WO}_3$  crystallites are much broader than that of the crystalline bulk  $\text{WO}_3$ , which reflects the nanoparticle (NP) dimension of the supported  $\text{WO}_3$  crystallites. In addition, the Raman band of the terminal  $\text{W}=\text{O}$  bond of the surface  $\text{WO}_x$  species further shifts from  $\sim 1015$  to  $\sim 1020$   $\text{cm}^{-1}$  with increasing surface  $\text{WO}_x$  density.

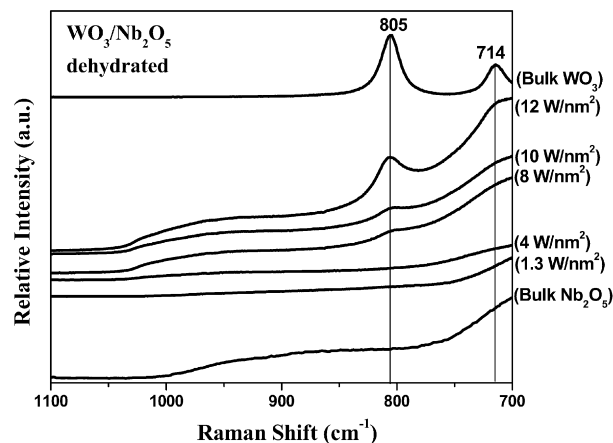


Fig. 2. Visible Raman spectra of the model-supported  $\text{WO}_3/\text{Nb}_2\text{O}_5$  catalysts under dehydrated conditions.

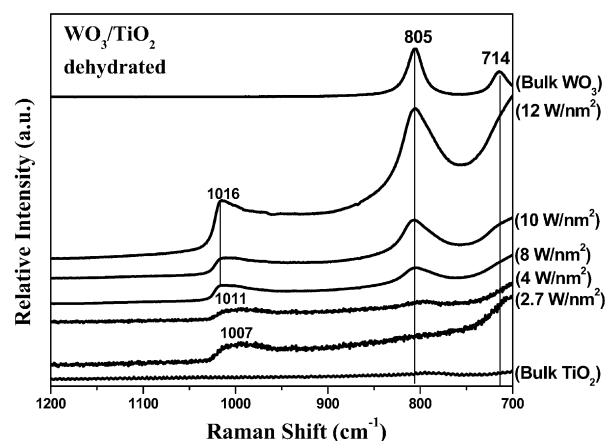


Fig. 3. Visible Raman spectra of the model-supported  $\text{WO}_3/\text{TiO}_2$  catalysts under dehydrated conditions.

### 3.2.2. Supported $\text{WO}_3/\text{Nb}_2\text{O}_5$ catalysts

The visible Raman spectra of the dehydrated supported  $\text{WO}_3/\text{Nb}_2\text{O}_5$  catalysts in the  $1.3$ – $12$   $\text{W}/\text{nm}^2$  range are presented in Fig. 2. The Raman spectra are limited to above  $700$   $\text{cm}^{-1}$  because of the strong Raman vibrations of the  $\text{Nb}_2\text{O}_5$  support below  $700$   $\text{cm}^{-1}$ . Crystalline  $\text{WO}_3$  NPs are not present in the  $1.3$ – $4$   $\text{W}/\text{nm}^2$  range and only appear at higher tungsten oxide surface density. Again, note that the supported  $\text{WO}_3$  NPs give rise to a broader Raman band at  $805$   $\text{cm}^{-1}$  than that for the corresponding bulk crystalline  $\text{WO}_3$  at higher tungsten oxide surface density ( $>4$   $\text{W}/\text{nm}^2$ ). The surface  $\text{WO}_x$  species give rise to a weak and broad Raman band in the  $900$ – $1000$   $\text{cm}^{-1}$  region against the  $\text{Nb}_2\text{O}_5$  support background that are further enhanced when the  $\text{Nb}_2\text{O}_5$  contribution is subtracted (not shown for brevity).

### 3.2.3. Supported $\text{WO}_3/\text{TiO}_2$ catalysts

The visible Raman spectra of dehydrated supported  $\text{WO}_3/\text{TiO}_2$  catalysts are shown in Fig. 3.

The Raman spectra are limited to above  $700$   $\text{cm}^{-1}$  because of the strong vibrations of the  $\text{TiO}_2$  support at lower values. In fact, the rising background below  $750$   $\text{cm}^{-1}$  is already a vi-

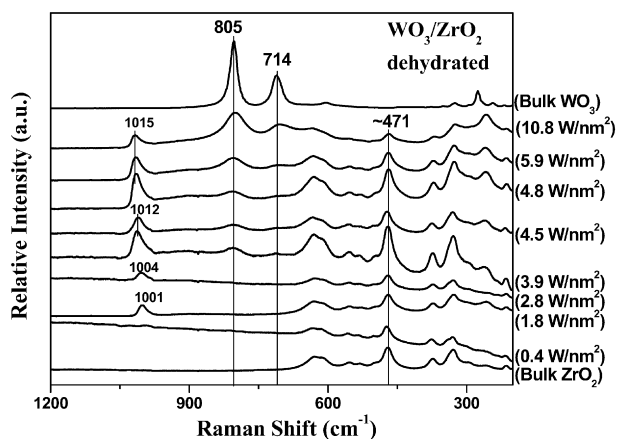


Fig. 4. Visible Raman spectra of the model-supported  $\text{WO}_3/\text{ZrO}_2$  catalysts under dehydrated conditions.

brational contribution from the  $\text{TiO}_2$  support. The dehydrated surface  $\text{WO}_x$  species gives rise to Raman bands in the  $\sim 1000$ – $1016 \text{ cm}^{-1}$  with increasing tungsten oxide surface coverage. This vibrational shift with tungsten oxide surface coverage is related to the continuous polymerization of the surface monotungstate species to surface polytungstate species [15]. The additional Raman band at  $\sim 805 \text{ cm}^{-1}$  at higher surface tungsten oxide density ( $>4 \text{ W/nm}^2$ ) reflects the presence of crystalline  $\text{WO}_3$  NPs.

### 3.2.4. Supported $\text{WO}_3/\text{ZrO}_2$ catalysts

The visible Raman spectra of the dehydrated supported  $\text{WO}_3/\text{ZrO}_2$  catalysts are presented in Fig. 4. The Raman spectrum for the  $0.4 \text{ W/nm}^2$  sample does not give rise to detectable bands for the surface  $\text{WO}_x$  species against the strong Raman spectrum of the  $\text{ZrO}_2$  support. The Raman band of the surface  $\text{WO}_x$  species shifts from  $1001$  to  $1015 \text{ cm}^{-1}$  with increasing surface  $\text{WO}_x$  coverage reflecting the transformation of surface monotungstate to polytungstate species. Crystalline  $\text{WO}_3$  NPs are present at  $\sim 4 \text{ W/nm}^2$  and higher surface density with Raman bands at  $805$  and  $714 \text{ cm}^{-1}$ .

### 3.2.5. Monolayer surface $\text{WO}_x$ coverage on oxide supports

Monolayer surface  $\text{WO}_x$  coverage for the supported  $\text{WO}_3/\text{ZrO}_2$  catalyst system was determined by using the strong  $\sim 471 \text{ cm}^{-1}$  band of the  $\text{ZrO}_2$  support as an internal standard. Two different methods were used to determine monolayer surface  $\text{WO}_x$  coverage. The first method plotted the intensity of the Raman band of the dehydrated surface  $\text{WO}_x$  species in the  $1000$ – $1020 \text{ cm}^{-1}$  region by normalizing this band to the  $\text{ZrO}_2$  internal standard as a function of tungsten oxide surface density. The normalized Raman intensity of the dehydrated surface  $\text{WO}_x$  species as a function of the tungsten oxide surface density on the  $\text{ZrO}_2$  support is presented in Fig. 5a. The normalized Raman intensity for the surface  $\text{WO}_x$  species linearly increases with  $\text{W/nm}^2$  and levels off at  $\sim 4.5 \text{ W/nm}^2$ . Note that no further increase in the normalized surface  $\text{WO}_x$  Raman intensity occurs above  $\sim 4.5 \text{ W/nm}^2$ , which reflects saturation of monolayer surface coverage of the surface  $\text{WO}_x$  species on  $\text{ZrO}_2$ . The second method plotted the normalized Raman intensity of

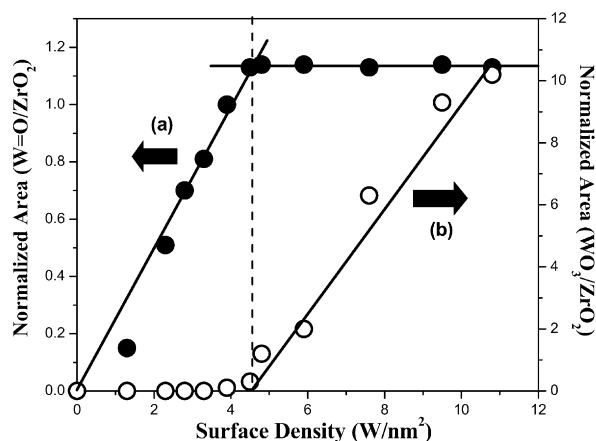


Fig. 5. Plots of normalized Raman intensity of the dehydrated surface  $\text{WO}_x$  species ( $\sim 1000$ – $1020 \text{ cm}^{-1}$ ) and crystalline  $\text{WO}_3$  particles ( $\sim 805 \text{ cm}^{-1}$ ) as a function of tungsten oxide surface density ( $\text{W/nm}^2$ ) on the model  $\text{ZrO}_2$  support.

the crystalline  $\text{WO}_3$  NPs ( $\sim 805 \text{ cm}^{-1}$ ) as a function of tungsten oxide surface density and is shown in Fig. 5b. The normalized crystalline  $\text{WO}_3$  NP Raman intensity is zero until  $\sim 4 \text{ W/nm}^2$  and then increases linearly with surface W density. Extrapolating the linear portion of the curve back to its intercept with the  $x$ -axis gives a value of  $\sim 4.5 \text{ W/nm}^2$ . This extrapolation method avoids considering the formation of small amounts of  $\text{WO}_3$  NPs that typically form as monolayer surface coverage is approached. Thus, both Raman methods quantitatively demonstrate that monolayer surface coverage occurs at  $\sim 4.5 \text{ W/nm}^2$  for the supported  $\text{WO}_3/\text{ZrO}_2$  catalyst system.

Comparison of the Raman spectra of the supported  $\text{WO}_3/\text{ZrO}_2$  catalysts with the other supported tungsten oxide catalysts also provides information about monolayer surface  $\text{WO}_x$  coverage on these other oxide supports. Crystalline  $\text{WO}_3$  NPs are not present below  $\sim 4 \text{ W/nm}^2$  on any of the supports and the intensity of the crystalline  $\text{WO}_3$  NPs increases with increasing  $\text{W/nm}^2$  above  $\sim 4 \text{ W/nm}^2$ . Furthermore, the appearance of crystalline  $\text{WO}_3$  NPs at  $\sim 4.5 \text{ W/nm}^2$  was also found to be independent of catalyst calcination temperature reflecting the universal value of  $\sim 4.5 \text{ W/nm}^2$  for monolayer surface  $\text{WO}_x$  coverage on oxide supports.

### 3.3. In situ UV–vis diffuse reflectance spectroscopy (DRS)

The UV–vis DRS  $E_g$  values for the dehydrated supported  $\text{WO}_3/\text{ZrO}_2$  (represented by open symbols) and  $\text{WO}_3/\text{Al}_2\text{O}_3$  (represented by solid symbols) are presented in Fig. 6 as functions of the tungsten oxide surface density ( $\text{W/nm}^2$ ) and calcination temperature. Recall that the UV–vis DRS for the supported  $\text{WO}_3/\text{TiO}_2$  and  $\text{WO}_3/\text{Nb}_2\text{O}_5$  were not collected because of the strong absorbance by the  $\text{TiO}_2$  and  $\text{Nb}_2\text{O}_5$  supports in the region of interest. Both supported tungsten oxide catalyst systems exhibit the same trend with increasing  $\text{W/nm}^2$  and essentially fall on the same curve. In addition, the data points for the supported  $\text{WO}_3/\text{ZrO}_2$  calcined at different temperatures also fall on the same curve. Thus, the UV–vis DRS  $E_g$  values are independent of the specific oxide support and calcination tem-

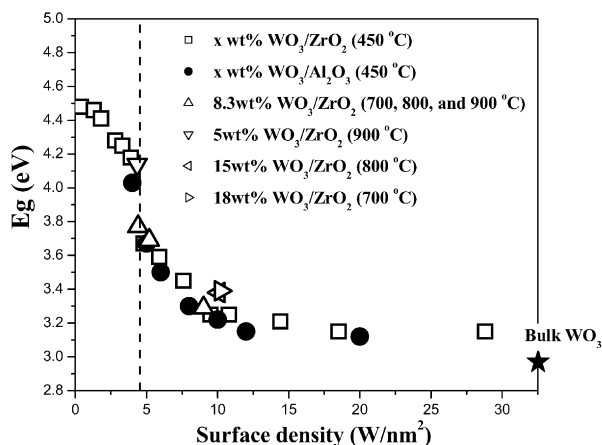
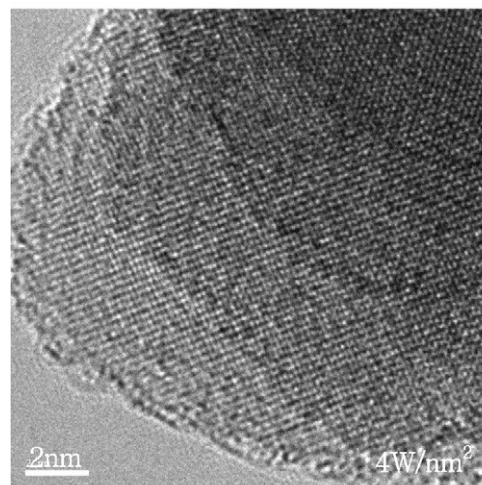


Fig. 6. Plot of UV-vis DRS  $E_g$  values for the dehydrated model-supported  $\text{WO}_3/\text{ZrO}_2$  and  $\text{WO}_3/\text{Al}_2\text{O}_3$  catalysts calcined at different temperatures as a function of tungsten oxide surface density ( $\text{W}/\text{nm}^2$ ).

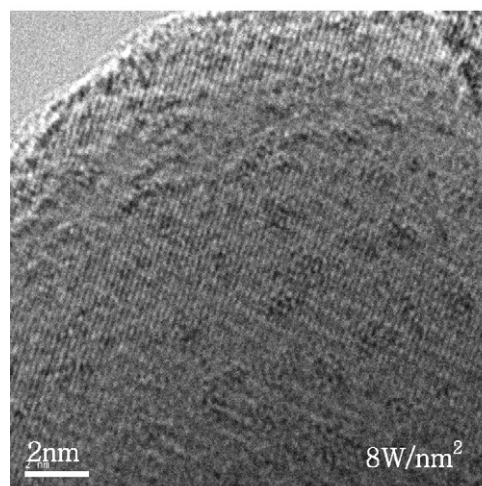
perature when plotted as a function of tungsten oxide surface density. The universal  $E_g$  vs tungsten oxide surface density plot exhibits three distinct regions: (1) modest decrease in  $E_g$  values between 0 and  $4.5 \text{ W}/\text{nm}^2$ , (2) somewhat greater decrease in  $E_g$  values between  $4.5$  and  $10 \text{ W}/\text{nm}^2$ , and (3) relatively constant  $E_g$  values above  $10 \text{ W}/\text{nm}^2$  that asymptotically approach the  $E_g$  value of large bulk  $\text{WO}_3$  crystals. The initial  $E_g$  values at the lowest surface coverage exhibit a value of  $\sim 4.5 \text{ eV}$  that continues to decrease with increasing surface  $\text{WO}_x$  coverage up to monolayer coverage of  $\sim 4.5 \text{ W}/\text{nm}^2$ . The initial  $E_g$  value is between the  $E_g$  values for isolated ( $\text{Na}_2\text{WO}_4$  at  $\sim 5.2 \text{ eV}$ ) and extensively polymerized ( $\text{Na}_2\text{W}_2\text{O}_7$  at  $4.2 \text{ eV}$ )  $\text{WO}_x$  structures suggesting a mixture of these two surface  $\text{WO}_x$  structures below monolayer surface coverage. Furthermore, the  $E_g$  value monotonically decreases with increasing surface W density up to monolayer coverage reflecting that the surface  $\text{WO}_x$  species are becoming more polymerized as the surface  $\text{WO}_x$  density increases in the submonolayer region. The  $E_g$  value at monolayer surface  $\text{WO}_x$  coverage corresponds to that of a linear  $\text{WO}_x$  polymer present [e.g.,  $(\text{NH}_4)_2\text{W}_2\text{O}_7$ ]. Above  $4.5 \text{ W}/\text{nm}^2$ , the  $E_g$  value continues to rapidly decrease and Raman simultaneously detects the presence of crystalline  $\text{WO}_3$  NPs in this tungsten oxide surface density region. The  $E_g$  values of the supported  $\text{WO}_3$  crystallites, however, are greater than that for large bulk  $\text{WO}_3$  crystallites, because they are present as  $\text{WO}_3$  NPs between  $4.5$  and  $10 \text{ W}/\text{nm}^2$ . Above  $10 \text{ W}/\text{nm}^2$ , the  $E_g$  values remain relatively constant with increasing surface W density, because the  $\text{WO}_3$  particles are much larger in this tungsten oxide surface density region and exhibit bulk-like characteristics. In summary, UV-vis DRS in combination with Raman spectroscopy is able to discriminate between isolated surface  $\text{WO}_x$  species, polymeric surface  $\text{WO}_x$  species,  $\text{WO}_3$  NPs and large bulk-like  $\text{WO}_3$  particles.

#### 3.4. High resolution-transmission electron microscopy (HR-TEM)

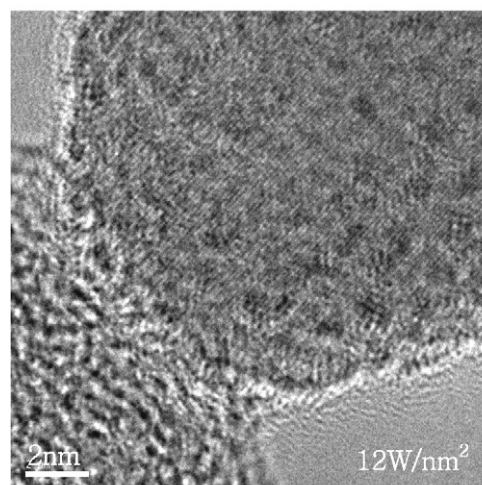
Representative HR-TEM images of the supported  $\text{WO}_3/\text{ZrO}_2$  catalysts are shown in Figs. 7a–7c for the catalysts with



(a)



(b)



(c)

Fig. 7. HR-TEM images of (a) 4, (b) 8, and (c)  $12 \text{ W}/\text{nm}^2$   $\text{WO}_3/\text{ZrO}_2$  catalysts.

a surface  $\text{W}/\text{ZrO}_2$  density of 4, 8, and  $12 \text{ W}/\text{nm}^2$ , respectively. All of the HR-TEM images obtained clearly display crystalline  $\text{ZrO}_2$  lattice fringes, especially at lower magnifications. The additional presence of an amorphous  $\text{WO}_x$  overlayer, and very

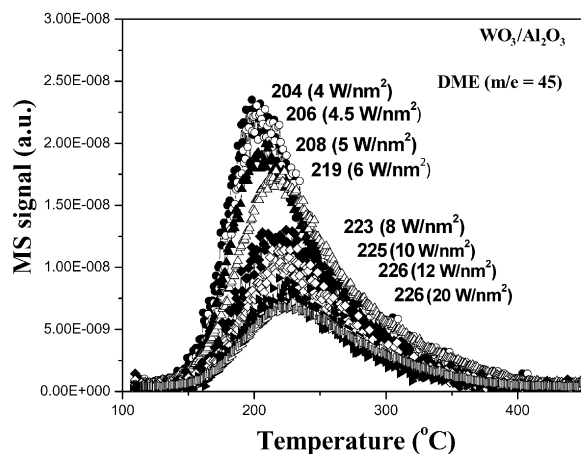


Fig. 8.  $\text{CH}_3\text{OH}$ -TPSR spectra for methanol dehydration to  $\text{CH}_3\text{OCH}_3$  over the model supported  $\text{WO}_3/\text{Al}_2\text{O}_3$  catalysts as a function of the tungsten oxide surface density ( $\text{W}/\text{nm}^2$ ).

small tungsten oxide NPs that are around 1 nm in size are also suggested by this sequence of images. The amorphous overlayer of the surface  $\text{WO}_x$  species appears most prominently at the edges of the support particles when viewed in profile. In addition, very small NPs possessing a lateral dimension of around 1 nm can be seen as darker flecks against the  $\text{ZrO}_2$  support, and appear by virtue of their mass contrast. A general trend of increasing number density of these dark flecks with increasing surface  $\text{W}/\text{nm}^2$  density was observed, although it is interesting to note that their average lateral size did not increase markedly with W loading. These dark flecks are thought to arise from the presence of crystalline  $\text{WO}_3$  nanoparticles and possibly also from hydrated  $(\text{WO}_x) \cdot n\text{H}_2\text{O}$  clusters. It should, however, be noted that the  $\text{WO}_x$  overlayers on these  $\text{ZrO}_2$  support particles are very sensitive to modification in the electron beam and great care needs to be taken to minimize the electron dose during HR-TEM imaging experiments.

### 3.5. $\text{CH}_3\text{OH}$ -TPSR spectroscopy

Methanol was used as a chemical probe molecule because it readily discriminates between surface acidic sites (formation of  $\text{CH}_3\text{OCH}_3$ ), basic sites (formation of  $\text{CO}/\text{CO}_2$ ), and redox sites (formation of  $\text{HCHO}$  and  $\text{CH}_3\text{OOCH}$ ). The supported  $\text{WO}_3$  catalysts exclusively yielded  $\text{CH}_3\text{OCH}_3$  as the reaction product during  $\text{CH}_3\text{OH}$ -TPSR demonstrating their surface acidic nature. The  $\text{CH}_3\text{OH}$ -TPSR spectra also allowed determination of the number of surface acid sites (reflected in the area underneath the DME curve) and the kinetics or strength of the surface acid sites (reflected by the  $T_p$  value). Furthermore, using the Redhead equation it was possible to directly determine the activation energy for the surface reaction ( $E_{\text{act}}$ ) in dimethyl ether formation and the kinetics for the rate-determining step ( $k_{\text{rds}}$ ), which involves the first-order C–O bond scission of the surface methoxy ( $\text{CH}_3\text{O}^*$ ) intermediate [31].

#### 3.5.1. Supported $\text{WO}_3/\text{Al}_2\text{O}_3$ catalysts

The DME/ $\text{CH}_3\text{OH}$ -TPSR spectra from the supported  $\text{WO}_3/\text{Al}_2\text{O}_3$  catalysts are shown in Fig. 8 and the  $T_p$  values are listed

Table 2  
DME/ $\text{CH}_3\text{OH}$ -TPSR  $T_p$  temperature ( $^\circ\text{C}$ ) for the supported  $\text{WO}_3$  catalysts on the model oxide supports ( $\text{TiO}_2$ ,  $\text{Nb}_2\text{O}_5$ ,  $\text{Al}_2\text{O}_3$ , and  $\text{ZrO}_2$ )

Sample (calcination temperature, $^\circ\text{C}$ )	Surface density ( $\text{W}/\text{nm}^2$ )	DME peak temperature ( $^\circ\text{C}$ )
Bulk $\text{TiO}_2$	0.0	325
7.3 wt% $\text{WTi}$ (450)	4.0	289
8.1 wt% $\text{WTi}$ (450)	4.5	289
13.6 wt% $\text{WTi}$ (450)	8.0	264
16.4 wt% $\text{WTi}$ (450)	10.0	260
19.1 wt% $\text{WTi}$ (450)	12.0	259
Bulk $\text{Nb}_2\text{O}_5$	0.0	300
9.2 wt% $\text{WNb}$ (450)	4.0	286
10.2 wt% $\text{WNb}$ (450)	4.5	286
16.9 wt% $\text{WNb}$ (450)	8.0	277
20.3 wt% $\text{WNb}$ (450)	10.0	272
23.4 wt% $\text{WNb}$ (450)	12.0	271
Bulk $\text{Al}_2\text{O}_3$		196
21.5 wt% $\text{WAl}$ (450)	4.0	204
23.5 wt% $\text{WAl}$ (450)	4.5	206
25.6 wt% $\text{WAl}$ (450)	5.0	208
29.1 wt% $\text{WAl}$ (450)	6.0	219
35.4 wt% $\text{WAl}$ (450)	8.0	223
40.7 wt% $\text{WAl}$ (450)	10.0	225
45.1 wt% $\text{WAl}$ (450)	12.0	226
57.8 wt% $\text{WAl}$ (450)	20.0	226
Bulk $\text{ZrO}_2$	0.0	374
3 wt% $\text{WZr}$ (450)	1.3	327
5 wt% $\text{WZr}$ (450)	2.3	319
6 wt% $\text{WZr}$ (450)	2.8	305
8.3 wt% $\text{WZr}$ (450)	4.0	297
9.4 wt% $\text{WZr}$ (450)	4.5	290
10 wt% $\text{WZr}$ (450)	4.8	286
15 wt% $\text{WZr}$ (450)	7.6	268
20 wt% $\text{WZr}$ (450)	10.8	266
25.0 wt% $\text{WZr}$ (450)	14.4	262
40.0 wt% $\text{WZr}$ (450)	28.9	259

in Table 2. The DME/ $\text{CH}_3\text{OH}$ -TPSR spectra exhibit increasing  $T_p$  values with increasing tungsten oxide surface density. The supported surface  $\text{WO}_x$  monolayer on alumina exhibits a  $T_p$  value of  $206^\circ\text{C}$  compared with  $196^\circ\text{C}$  for the  $\text{WO}_3$ -free  $\text{Al}_2\text{O}_3$  support and  $254^\circ\text{C}$  for bulk  $\text{WO}_3$ . The absence of a DME-TPSR peak at  $196^\circ\text{C}$  reveals that exposed alumina supports sites are not present at monolayer surface  $\text{WO}_x$  coverage. Increasing the tungsten oxide surface density above monolayer coverage further increases the  $T_p$  temperature from 206 to  $226^\circ\text{C}$  indicating that the crystalline  $\text{WO}_3$  NPs present in this tungsten oxide surface density region are less active than the surface  $\text{WO}_x$  monolayer on  $\text{Al}_2\text{O}_3$  for the acid catalyzed methanol dehydration reaction. Thus, the surface  $\text{WO}_x$  monolayer on  $\text{Al}_2\text{O}_3$  is more reactive than  $\text{WO}_3$  NPs and bulk  $\text{WO}_3$ . In addition to these reactivity changes with tungsten oxide surface density, the number of catalytic active sites monotonically decreases above monolayer tungsten oxide surface coverage with increasing  $\text{W}/\text{nm}^2$  reflecting the presence of less dispersed crystalline  $\text{WO}_3$  NPs.

#### 3.5.2. Supported $\text{WO}_3/\text{ZrO}_2$ catalysts

The DME/ $\text{CH}_3\text{OH}$ -TPSR spectra for the supported  $\text{WO}_3/\text{ZrO}_2$  catalysts are presented in Fig. 9 and listed in Table 2.

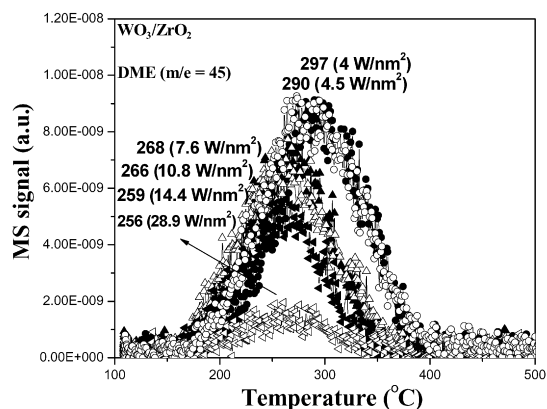


Fig. 9. CH<sub>3</sub>OH-TPSR spectra for methanol dehydration to DME over the model supported WO<sub>3</sub>/ZrO<sub>2</sub> catalysts as a function of tungsten oxide surface density (W/nm<sup>2</sup>).

In contrast to the supported WO<sub>3</sub>/Al<sub>2</sub>O<sub>3</sub> catalyst system that exhibits an increase in DME/CH<sub>3</sub>OH-TPSR Tp values with increasing W/nm<sup>2</sup>, the supported WO<sub>3</sub>/ZrO<sub>2</sub> catalysts exhibit a decrease in DME/CH<sub>3</sub>OH-TPSR Tp values with increasing W/nm<sup>2</sup>. The surface WO<sub>x</sub> monolayer on ZrO<sub>2</sub> exhibits a Tp value of 290 °C that is greater than crystalline bulk WO<sub>3</sub> at 254 °C and less than the WO<sub>3</sub>-free ZrO<sub>2</sub> support at 374 °C. At high tungsten oxide surface density, the Tp value approaches that of bulk WO<sub>3</sub> particles. Thus, the crystalline WO<sub>3</sub> NPs are more active than the surface WO<sub>x</sub> monolayer on the ZrO<sub>2</sub> support and dominate the catalytic properties at high tungsten oxide surface density. Furthermore, the number of catalytic active sites decreases with increasing tungsten oxide surface density above monolayer surface coverage because of the presence of crystalline WO<sub>3</sub> NPs above monolayer coverage.

### 3.5.3. Supported WO<sub>3</sub>/Nb<sub>2</sub>O<sub>5</sub> catalysts

The DME/CH<sub>3</sub>OH-TPSR spectra for the supported WO<sub>3</sub>/Nb<sub>2</sub>O<sub>5</sub> catalysts follow a similar trend as that for supported WO<sub>3</sub>/ZrO<sub>2</sub> and are not shown for brevity. The DME/CH<sub>3</sub>OH-TPSR Tp values for the supported WO<sub>3</sub>/Nb<sub>2</sub>O<sub>5</sub> catalysts are listed in Table 2 and the Tp values decrease with increasing tungsten oxide surface density. The Tp value for the surface WO<sub>x</sub> monolayer on Nb<sub>2</sub>O<sub>5</sub> is 286 °C, which is higher than that for bulk WO<sub>3</sub> at 254 °C and less than that for the WO<sub>3</sub>-free Nb<sub>2</sub>O<sub>5</sub> support at 300 °C. Increasing the tungsten oxide surface density on Nb<sub>2</sub>O<sub>5</sub> above monolayer surface WO<sub>x</sub> coverage further decreases the Tp values from 286 to 271 °C, which reveals that the WO<sub>3</sub> NPs are more active than the surface WO<sub>x</sub> species anchored to the Nb<sub>2</sub>O<sub>5</sub> support. As for the supported WO<sub>3</sub>/Al<sub>2</sub>O<sub>3</sub> and WO<sub>3</sub>/ZrO<sub>2</sub> catalyst systems, the number of catalytic active sites decreases with increasing tungsten oxide surface density above monolayer surface WO<sub>x</sub> coverage on Nb<sub>2</sub>O<sub>5</sub>.

### 3.5.4. Supported WO<sub>3</sub>/TiO<sub>2</sub> catalysts

The DME/CH<sub>3</sub>OH-TPSR spectra for the supported WO<sub>3</sub>/TiO<sub>2</sub> catalysts follow the trends found for the supported WO<sub>3</sub>/ZrO<sub>2</sub> and WO<sub>3</sub>/Nb<sub>2</sub>O<sub>5</sub> catalyst systems and are not shown for brevity. The associated Tp values are listed in Ta-

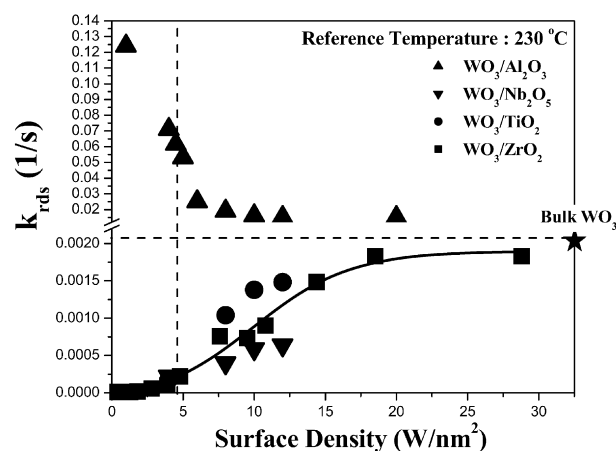


Fig. 10. First-order kinetic rate constants,  $k_{rds}$ , for CH<sub>3</sub>OH dehydration to DME over the model-supported WO<sub>3</sub> catalysts as a function of tungsten oxide surface density (W/nm<sup>2</sup>).

ble 2 and the Tp values decrease with increasing tungsten oxide surface density. The monolayer surface WO<sub>x</sub> species on TiO<sub>2</sub> exhibits a Tp value of 289 °C compared with 254 °C for bulk WO<sub>3</sub> and 325 °C for the WO<sub>3</sub>-free TiO<sub>2</sub> support. The activity of the monolayer surface WO<sub>x</sub> monolayer on TiO<sub>2</sub> is comparable to that of the surface WO<sub>x</sub> monolayer on Nb<sub>2</sub>O<sub>5</sub> and ZrO<sub>2</sub>, but at higher surface density, the supported WO<sub>3</sub>/TiO<sub>2</sub> catalyst system is slightly more active than the supported WO<sub>3</sub>/Nb<sub>2</sub>O<sub>5</sub> and WO<sub>3</sub>/ZrO<sub>2</sub> catalyst systems. As for the other supported WO<sub>3</sub> catalysts, the number of catalytic active sites decreases with increasing tungsten oxide surface density above monolayer surface WO<sub>x</sub> coverage because of the presence of crystalline WO<sub>3</sub> NPs.

### 3.5.5. Comparison of DME/CH<sub>3</sub>OH-TPSR results for the supported WO<sub>3</sub> catalysts

The first-order  $k_{rds}$  kinetic rate constants for methanol dehydration to dimethyl ether over the supported WO<sub>3</sub> catalysts at 230 °C are plotted in Fig. 10 as a function of tungsten oxide surface density. The kinetic  $k_{rds}$  values were determined from the DME/CH<sub>3</sub>OH-TPSR Tp values and application of the Redhead equation (see Section 2.5 above for details). The supported WO<sub>3</sub>/TiO<sub>2</sub>, WO<sub>3</sub>/Nb<sub>2</sub>O<sub>5</sub>, and WO<sub>3</sub>/ZrO<sub>2</sub> catalyst systems follow the exact same  $k_{rds}$  trend, increasing as a function of W/nm<sup>2</sup> and approach the activity value of bulk WO<sub>3</sub> at high W/nm<sup>2</sup> values. In contrast, the supported WO<sub>3</sub>/Al<sub>2</sub>O<sub>3</sub> catalyst system follows an inverse  $k_{rds}$  trend, decreasing as a function of W/nm<sup>2</sup> and does not approach the value of bulk WO<sub>3</sub> at high W/nm<sup>2</sup> values. Even at the highest tungsten oxide surface density, the supported WO<sub>3</sub>/Al<sub>2</sub>O<sub>3</sub> catalysts are about an order of magnitude more active than bulk WO<sub>3</sub> and the other supported WO<sub>3</sub> catalysts. The initial high  $k_{rds}$  values for supported WO<sub>3</sub>/Al<sub>2</sub>O<sub>3</sub> below monolayer surface coverage are related to exposed alumina sites, but all of the alumina sites are covered with the surface WO<sub>x</sub> monolayer at monolayer surface coverage and higher W/nm<sup>2</sup>. This suggests that the surface WO<sub>x</sub> species coordinated to the Al<sub>2</sub>O<sub>3</sub> surface are highly active acid sites and even more active than the supported WO<sub>3</sub> NPs for methanol dehydration.

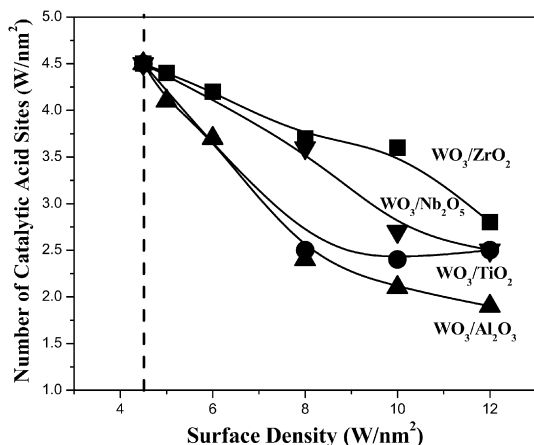


Fig. 11. Number of catalytic active sites for the model-supported WO<sub>3</sub> catalysts as a function of tungsten oxide surface density (W/nm<sup>2</sup>).

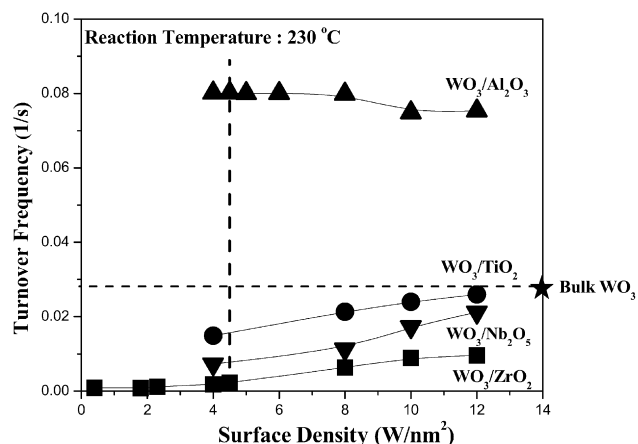


Fig. 12. Catalytic acidity TOF values for CH<sub>3</sub>OH dehydration to DME over the model-supported WO<sub>3</sub> catalysts as function of tungsten oxide surface density (W/nm<sup>2</sup>).

The number of catalytic active sites for the supported WO<sub>3</sub> catalysts is plotted as a function of W/nm<sup>2</sup> in Fig. 11. For all supported WO<sub>3</sub> catalyst systems, the number of catalytic active sites decreases with W/nm<sup>2</sup> above monolayer coverage because of the presence of crystalline WO<sub>3</sub> NPs on top of the surface WO<sub>x</sub> monolayer in this coverage region. The slight differences in the decrease in  $N_s$  with W/nm<sup>2</sup> for the different supported WO<sub>3</sub> catalyst systems may be related to the different surface areas and pore structures of the oxide supports.

### 3.6. Steady-state methanol dehydration kinetics

The turnover frequency (TOF) values (methanol molecules dehydrated per exposed tungsten oxide site per second) for the supported WO<sub>3</sub> catalysts at 230 °C are presented in Fig. 12 as a function of the W/nm<sup>2</sup>. The TOF values were determined from knowledge of the number of catalytic active sites obtained from the CH<sub>3</sub>OH-TPSR spectra shown in Fig. 11. The relative TOF values of the surface acidic catalytic active sites at monolayer surface WO<sub>x</sub> coverage follow the trend WO<sub>3</sub>/Al<sub>2</sub>O<sub>3</sub> ≫ bulk WO<sub>3</sub> > WO<sub>3</sub>/TiO<sub>2</sub> > WO<sub>3</sub>/Nb<sub>2</sub>O<sub>5</sub> > WO<sub>3</sub>/ZrO<sub>2</sub>. The pres-

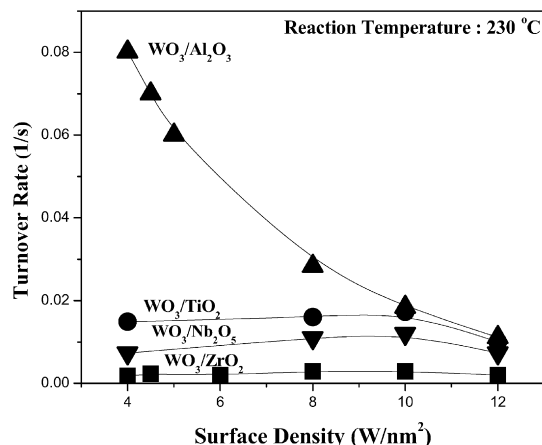


Fig. 13. Catalytic acidity TOR values for CH<sub>3</sub>OH dehydration to DME over the model-supported WO<sub>3</sub> catalysts as a function of tungsten oxide surface density (W/nm<sup>2</sup>).

ence of WO<sub>3</sub> NPs above monolayer surface coverage further alters the TOF values. For the supported WO<sub>3</sub>/Al<sub>2</sub>O<sub>3</sub> catalyst system, the TOF value decreases above monolayer surface coverage because of the lower activity of the WO<sub>3</sub> NPs relative to the surface WO<sub>x</sub> sites anchored to the alumina support. For the supported WO<sub>3</sub>/TiO<sub>2</sub>, WO<sub>3</sub>/Nb<sub>2</sub>O<sub>5</sub>, and WO<sub>3</sub>/ZrO<sub>2</sub> catalyst systems, the TOF increases above monolayer surface coverage because of the higher activity of the WO<sub>3</sub> NPs compared with the surface WO<sub>x</sub> species coordinated to these oxide supports. The TOF values of the nonalumina-supported tungsten oxide catalysts asymptotically approach the TOF value of bulk WO<sub>3</sub> at very high W/nm<sup>2</sup> values. The TOF value of the supported WO<sub>3</sub>/Al<sub>2</sub>O<sub>3</sub> catalyst system, however, remains much higher than the TOF for bulk WO<sub>3</sub> at high W/nm<sup>2</sup>. The different trends reflect the contributions of the surface WO<sub>x</sub> monolayer relative to WO<sub>3</sub> NPs toward methanol dehydration.

The turnover rates (TOR), number of methanol molecules dehydrated per all W oxide atoms in the catalyst per second, of the supported WO<sub>3</sub> catalysts as a function of W/nm<sup>2</sup> at 230 °C are presented in Fig. 13. For the submonolayer region, the TOF and TOR values are identical because the supported tungsten oxide is 100% dispersed on the supports. Above monolayer surface coverage, TOF is always greater than TOR because the supported tungsten oxide phase is not 100% dispersed on the supports. The poorly dispersed crystalline WO<sub>3</sub> NPs are also present above monolayer surface coverage and decrease the TOR values because all of the W oxide atoms are used in normalizing the reaction rate. The maximum TOR values for the supported WO<sub>3</sub> catalysts, with the exception of supported WO<sub>3</sub>/Al<sub>2</sub>O<sub>3</sub>, occurs at ~8–10 W/nm<sup>2</sup>. At higher W/nm<sup>2</sup> values (>10 W/nm<sup>2</sup>), the TOR values for all of the supported WO<sub>3</sub> catalyst systems asymptotically approach the same value. The similar TOR value at high W/nm<sup>2</sup> is a consequence of the predominance of the bulk-like WO<sub>3</sub> crystallites and their associated low dispersion at these high tungsten oxide surface density values.

A more detailed comparison of TOR and TOF values is shown for the supported WO<sub>3</sub>/ZrO<sub>2</sub> catalyst system in Fig. 14 (note that the y-scales are different for TOR and TOF). The

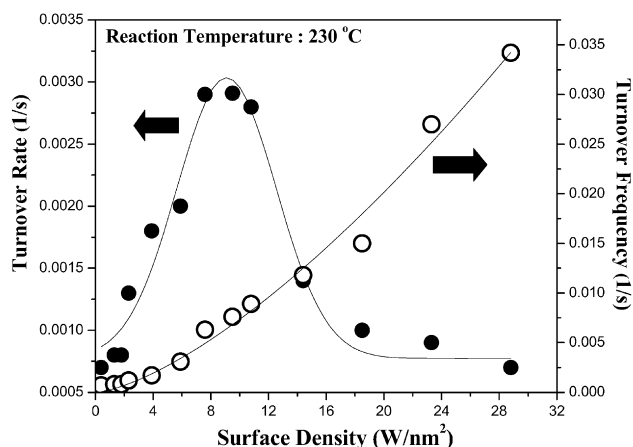


Fig. 14. Comparison of catalytic acidity TOR and TOF values for the model-supported  $\text{WO}_3/\text{ZrO}_2$  catalysts as a function of tungsten oxide surface density ( $\text{W}/\text{nm}^2$ ).

TOF and TOR values increase continuously with increasing  $\text{W}/\text{nm}^2$  below monolayer coverage. The similar TOF and TOR trend is related to the 100% dispersion of the supported tungsten oxide phase in the submonolayer region. The increasing TOF and TOR values with surface tungsten oxide density ( $\text{W}/\text{nm}^2$ ) below monolayer coverage reflect the greater catalytic acidity of the surface polytungstate species compared with the surface monotungstate species. The further increase in TOF and TOR values between 5 and 10  $\text{W}/\text{nm}^2$  demonstrates that the  $\text{WO}_3$  NPs are more active than the surface  $\text{WO}_x$  species. Above 10  $\text{W}/\text{nm}^2$ , the low dispersion of the bulk-like  $\text{WO}_3$  particles significantly decreases the TOR values as the TOF values continue to increase. The continued increase of the TOF catalytic acidity values reflects the higher specific catalytic acidity of the bulk-like  $\text{WO}_3$  particles relative to the  $\text{WO}_3$  NPs.

## 4. Discussion

### 4.1. Tungsten oxide monolayer surface coverage

The Raman spectra of the supported  $\text{WO}_3$  catalysts quantitatively demonstrate that tungsten oxide monolayer surface coverage on the model oxide supports corresponds to  $\sim 4.5 \text{ W}/\text{nm}^2$ . Below  $\sim 4.5 \text{ W}/\text{nm}^2$ , surface  $\text{WO}_x$  species predominate, and only minor amounts of crystalline  $\text{WO}_3$  NPs are present as monolayer surface coverage is approached (see Figs. 1–5). From corresponding X-ray photoelectron spectroscopy (XPS) surface analysis of the surface  $\text{W}/\text{Zr}$  ratio as a function of  $\text{W}/\text{nm}^2$  for the same model-supported  $\text{WO}_3/\text{ZrO}_2$  catalysts, monolayer surface coverage was determined to occur at  $\sim 4.8 \text{ W}/\text{nm}^2$  [35]. The conclusion that the tungsten oxide monolayer surface coverage on model oxide supports corresponds to  $\sim 4.5\text{--}4.8 \text{ W}/\text{nm}^2$  is in agreement with almost all previous monolayer surface coverage determinations that for model-supported  $\text{WO}_3$  catalysts monolayer coverage corresponds to  $\sim 4\text{--}5 \text{ W}/\text{nm}^2$  and is independent of the specific oxide support with the exception of the weakly interacting supported  $\text{WO}_3/\text{SiO}_2$  catalyst system [15,17,21,24,25,36–50].

### 4.2. Molecular and electronic structures of the supported tungsten oxide phases

All of the supported  $\text{WO}_3$  catalysts exhibit Raman bands for the dehydrated surface  $\text{WO}_x$  species between  $\sim 1000$  and  $1020 \text{ cm}^{-1}$  as the tungsten oxide surface density is increased in the submonolayer coverage region (see Figs. 1–4). The corresponding UV–vis DRS Eg values for supported  $\text{WO}_3/\text{Al}_2\text{O}_3$  and  $\text{WO}_3/\text{ZrO}_2$  catalyst systems decrease simultaneously with increasing tungsten oxide surface density, reflecting an increase in extent of polymerization of the surface  $\text{WO}_x$  species with increasing surface coverage (see Fig. 6). The simultaneous increase in the Raman vibrational band position of the terminal  $\text{W}=\text{O}$  bond and the decrease in UV–vis DRS Eg values for the supported  $\text{WO}_3/\text{Al}_2\text{O}_3$  and  $\text{WO}_3/\text{ZrO}_2$  catalyst systems reflect the polymerization of the surface  $\text{WO}_x$  species with surface coverage on these model oxide supports. Although the UV–vis DRS Eg values cannot be obtained for the supported  $\text{WO}_3/\text{TiO}_2$  and  $\text{WO}_3/\text{Nb}_2\text{O}_5$  catalyst systems, the Raman shift from  $\sim 1000$  to  $1016 \text{ cm}^{-1}$  also reflects the polymerization of the surface  $\text{WO}_x$  species on these model oxide supports, especially supported  $\text{WO}_3/\text{TiO}_2$ , with increasing tungsten oxide surface density. Consequently, the surface  $\text{WO}_x$  species progressively polymerize with increasing tungsten oxide surface density in the submonolayer region on these model oxide supports.

Above monolayer surface coverage of the 2D surface  $\text{WO}_x$  phase, 3D crystalline  $\text{WO}_3$  NPs are present between  $\sim 5$  and  $\sim 10 \text{ W}/\text{nm}^2$ . Raman readily detects the crystalline  $\text{WO}_3$  phase because of the significantly stronger Raman cross-section of bulk  $\text{WO}_3$  crystals than the surface  $\text{WO}_x$  species [34]. The HR-TEM images reveal that the supported crystalline  $\text{WO}_3$  particles on  $\text{ZrO}_2$  are on the order of  $\sim 1 \text{ nm}$  in size between 5 and 12  $\text{W}/\text{nm}^2$ . The NP dimension of the supported crystalline  $\text{WO}_3$  phase is also reflected in both its broader Raman bands and higher Eg values relative to large bulk  $\text{WO}_3$  crystals. At very high tungsten oxide surface density, the crystalline  $\text{WO}_3$  NPs are larger and begin to reflect the electronic structural characteristic of large bulk crystalline  $\text{WO}_3$  particles.

### 4.3. Number of exposed surface catalytic active acid sites

The number of surface acid sites was quantitatively determined from the amount of DME formed during the  $\text{CH}_3\text{OH}$ -TPSR experiment (see Fig. 11). Below tungsten oxide monolayer surface coverage ( $< 5 \text{ W}/\text{nm}^2$ ), the number of surface acid sites increases linearly with the tungsten oxide surface density. Above monolayer surface coverage, the number of exposed surface acid sites continuously decreases with tungsten oxide surface density on all of the supports because of the presence of crystalline  $\text{WO}_3$  NPs. The crystalline  $\text{WO}_3$  NPs reside on top of the surface  $\text{WO}_x$  monolayer and also cover up some of the surface  $\text{WO}_x$  acid sites. The trend in the quantitative decrease in the number of surface acid sites varies only slightly with tungsten oxide surface density among the different oxide supports. Furthermore, above tungsten oxide monolayer surface cover-

age, the surface acid sites are associated with both the surface  $\text{WO}_x$  species and the  $\text{WO}_3$  NPs.

#### 4.4. Relative catalytic acidity of surface $\text{WO}_x$ species and crystalline $\text{WO}_3$

The relative catalytic acidity of the surface monotungstate and polytungstate  $\text{WO}_x$  species and the  $\text{WO}_3$  NPs is dependent on the specific oxide support and was determined by the kinetics of DME formation during  $\text{CH}_3\text{OH}$ -TPSR (see Fig. 10). For all of the supports investigated, the surface polytungstate  $\text{WO}_x$  species are more acidic than the surface monotungstate  $\text{WO}_x$  species. This is reflected in the higher catalytic acid activity of the monolayer surface coverage catalysts with the corresponding submonolayer surface coverage catalysts. The catalytic acid activity of the submonolayer-supported  $\text{WO}_3/\text{Al}_2\text{O}_3$  catalyst could not be determined because the exposed surface Al sites were very active and overwhelmed the surface reactivity of the surface monotungstate  $\text{WO}_x$  species at low surface coverage.

For the supported  $\text{WO}_3/\text{Al}_2\text{O}_3$  catalytic system, the surface  $\text{WO}_x$  species at monolayer coverage are more acidic than the  $\text{WO}_3$  NPs. The supported  $\text{WO}_3$  NPs are more acidic than the surface  $\text{WO}_x$  species for the supported  $\text{WO}_3/\text{Nb}_2\text{O}_5$ ,  $\text{WO}_3/\text{TiO}_2$ , and  $\text{WO}_3/\text{ZrO}_2$  catalytic systems, however. This reveals the important contribution of the specific oxide support to the acidic character of the surface  $\text{WO}_x$  species. The catalytic acidity at tungsten oxide monolayer surface coverage increases with increasing support cation electronegativity (cation electronegativity,  $\text{Zr} < \text{Nb} \sim \text{Ti} < \text{Al}$ ) [51]. The greater the support cation electronegativity, the less electron density resides on the bridging W–O–support bond (less basic and more acidic). This reflects the ability of the support cation to tune the acidic character of the surface  $\text{WO}_x$  species relative to the  $\text{WO}_3$  NPs. With the exception of the supported  $\text{WO}_3/\text{Al}_2\text{O}_3$  catalytic system, which has an extremely acidic surface  $\text{WO}_x$  monolayer, the large  $\text{WO}_3$  particles present on  $\text{Nb}_2\text{O}_5$ ,  $\text{TiO}_2$ , and  $\text{ZrO}_2$  are more acidic than the surface  $\text{WO}_x$  species and the  $\text{WO}_3$  NPs.

#### 4.5. Steady-state TOF catalytic acidity values

For the supported  $\text{WO}_3/\text{Al}_2\text{O}_3$  catalyst system, the TOF catalytic acidity values slightly decreased above tungsten oxide monolayer surface coverage because of the less acidic  $\text{WO}_3$  NPs relative to the surface  $\text{WO}_x$  monolayer ( $\text{TOF}_{\text{Polytungstate}} > \text{TOF}_{\text{WO}_3, \text{NPs}}$ ). However, the TOF catalytic acidity values increased continuously with tungsten oxide surface density for supported  $\text{WO}_3/\text{Nb}_2\text{O}_5$ ,  $\text{WO}_3/\text{TiO}_2$ , and  $\text{WO}_3/\text{ZrO}_2$ , indicating that  $\text{TOF}_{\text{Monotungstate}} < \text{TOF}_{\text{Polytungstate}} < \text{WO}_3, \text{NPs} < \text{WO}_3, \text{Bulk}$ . Thus, the overall TOF catalytic acidity depends on the intrinsic catalytic acidity of the surface  $\text{WO}_x$  species and the  $\text{WO}_3$  NPs, as well as on their relative contributions to the total number of exposed surface acid sites. Consequently, there is no standard relationship between the tungsten oxide domain size and the specific catalytic acidity because of the significant role of the specific oxide support ligand on the acidity of the surface  $\text{WO}_x$  species.

#### 4.6. Steady-state TOR catalytic acidity values

The steady-state TOR catalytic acidity values are sometimes also reported in the catalysis literature because the actual number of exposed surface tungsten oxide sites is not determined. As a result, the reaction rate data are normalized by all of the atoms present in the supported metal oxide phase, all of the W oxide atoms in supported  $\text{WO}_3$  catalysts. Consequently, the actual dispersion of the supported  $\text{WO}_3$  phase is not taken into consideration. The current study with the model-supported  $\text{WO}_3$  catalysts allows a direct comparison between steady-state TOF and TOR values for the same catalysts and reaction where the dispersion of the supported  $\text{WO}_3$  phase is known. The steady-state TOR and TOF catalytic acidity values for  $\text{CH}_3\text{OH}$  dehydration are identical in the submonolayer region and at monolayer surface coverage because the supported  $\text{WO}_3$  phase is 100% dispersed as surface  $\text{WO}_x$  species on the oxide support. Above tungsten oxide monolayer surface coverage, the TOR and TOF catalytic acidity values begin to deviate because the presence of 3D crystalline  $\text{WO}_3$  NPs decreases the supported  $\text{WO}_3$  dispersion. As a result, the TOF catalytic acidity values will always be greater than the corresponding TOR catalytic acidity values because TOR overcounts the number of actual exposed catalytic acid sites above monolayer surface coverage. This overcounting of exposed catalytic active sites in the determination of TOR results in decreasing the TOR catalytic acidity values at high tungsten oxide surface density.

For the supported  $\text{WO}_3/\text{Al}_2\text{O}_3$  catalysts above monolayer coverage, the TOR catalytic acidity values decrease with increasing  $\text{W}/\text{nm}^2$  because of the overcounting of the exposed surface sites and the lower intrinsic catalytic acidity of the  $\text{WO}_3$  NPs (see Fig. 13). As mentioned earlier, the TOR catalytic acidity values for the supported  $\text{WO}_x$  species on  $\text{Al}_2\text{O}_3$  cannot be determined below monolayer coverage because of the much greater catalytic acidity of the exposed surface Al sites in the submonolayer region.

For the other supported  $\text{WO}_3$  model catalysts (supported  $\text{WO}_3/\text{Nb}_2\text{O}_5$ ,  $\text{WO}_3/\text{TiO}_2$ , and  $\text{WO}_3/\text{ZrO}_2$ ), the TOR catalytic acidity values increase between  $\sim 5$  and  $10 \text{ W}/\text{nm}^2$  because of the much higher intrinsic catalytic acidity of the  $\text{WO}_3$  NPs relative to the surface  $\text{WO}_x$  species (see Figs. 13 and 14), while the number of actual catalytic active sites decreases by only less than a factor of 2 (see Fig. 12). For tungsten oxide surface density  $> 10 \text{ W}/\text{nm}^2$ , the decrease in the number of actual catalytic acid sites is greater than the modest increase in catalytic acidity from the bulk-like  $\text{WO}_3$  particles and, thus, results in an overall decrease in TOR catalytic acidity values. Consequently, the initial increase and subsequent decrease of the TOR catalytic acidity values with  $\text{W}/\text{nm}^2$  above monolayer coverage is just a consequence of (i) the relative intrinsic catalytic activity of the  $\text{WO}_3$  NPs and the surface  $\text{WO}_x$  monolayer, (ii) the partition of exposed catalytic acidic sites between the  $\text{WO}_3$  NPs and the surface  $\text{WO}_x$  species, and (iii) ratio of actual number of exposed catalytic acid sites and the total number of W oxide atoms in the supported tungsten oxide phase. Thus, the maximum in the TOR catalytic acidity values with  $\text{W}/\text{nm}^2$  for model-supported  $\text{WO}_3/\text{ZrO}_2$ ,  $\text{WO}_3/\text{Nb}_2\text{O}_5$ , and  $\text{WO}_3/\text{TiO}_2$  catalysts is primarily

a consequence of overcounting the actual number of catalytic acidic sites present in supported  $\text{WO}_3$  catalysts at high  $\text{W}/\text{nm}^2$  values.

## 5. Conclusion

The nature of the dehydrated surface tungsten oxide phase is found to be the same on the different supports examined ( $\text{Al}_2\text{O}_3$ ,  $\text{ZrO}_2$ ,  $\text{TiO}_2$ , and  $\text{Nb}_2\text{O}_5$ ) as a function of  $\text{W}/\text{nm}^2$ . In the submonolayer region ( $<5 \text{ W}/\text{nm}^2$ ), both monotungstate and polytungstate surface  $\text{WO}_x$  species are present, and the ratio of polytungstate/monotungstate increases with tungsten oxide surface coverage. Above monolayer coverage ( $>5 \text{ W}/\text{nm}^2$ ), 3D crystalline  $\text{WO}_3$  NPs are present on top of the 2D surface  $\text{WO}_x$  monolayer. Above  $\sim 10 \text{ W}/\text{nm}^2$ , bulk-like  $\text{WO}_3$  large particles are also present. These different molecular structures of the supported tungsten oxide phase affect the overall dispersion of the supported  $\text{WO}_3$  catalysts. The dispersion is 100% in the submonolayer region and decreases continuously with increasing tungsten oxide loading above monolayer coverage due to the presence of the crystalline  $\text{WO}_3$  particles.

The relative catalytic acidity of the different tungsten oxide components depends on the specific oxide support. For supported  $\text{WO}_3/\text{Al}_2\text{O}_3$  catalysts, the surface  $\text{WO}_x$  species are more active than the crystalline  $\text{WO}_3$  particles. For the other supported  $\text{WO}_3$  catalysts, however, the crystalline  $\text{WO}_3$  particles are more active than the surface  $\text{WO}_x$  species. These different catalytic acidity patterns of the different tungsten oxide structures reflect the important effect of the specific oxide support on the relative acidic activity of the surface  $\text{WO}_x$  species to the  $\text{WO}_3$  NPs. As the support cation electronegativity increases ( $\text{Al} > \text{Nb} \sim \text{Ti} > \text{Zr}$ ), the electron density of the bridging  $\text{W}-\text{O}$ -support bond decreases and results in a more acidic site. Consequently, there is no general relationship between the tungsten oxide structure/domain size and the specific catalytic acidity.

## Acknowledgment

Support from the U.S. Department of Energy, Division of Basic Energy Sciences (Grant DE-FG 02-93 ER 14350) is gratefully acknowledged.

## References

- [1] C.L. Thomas, *Catalytic Processes and Proven Catalysts*, Academic Press, New York, 1970.
- [2] C.N. Satterfield, *Heterogeneous Catalysis in Practice*, McGraw-Hill, New York, 1980.
- [3] L.L. Murrell, C.J. Kim, D.C. Grenoble, US Patent 4 233 139 (1980).
- [4] D.C. Grenoble, C.J. Kim, L.L. Murrell, US Patent 4 440 872 (1984).
- [5] J. Bernholc, J.A. Horsley, L.L. Murrell, L.G. Sherman, S. Soled, *J. Phys. Chem.* 91 (1987) 1526.
- [6] L.L. Murrell, D.C. Grenoble, C.J. Kim, N.C. Dispenziere, *J. Catal.* 107 (1987) 463.
- [7] C. Wivel, B.S. Clausen, R. Candia, S. Morup, H. Topsøe, *J. Catal.* 87 (1984) 497.
- [8] I.E. Wachs, C.C. Chersich, J. Hardenbergh, *Appl. Catal.* 13 (1985) 335.
- [9] M. Ai, *J. Catal.* 49 (1977) 305.
- [10] S. Morikawa, K. Takahashi, J. Mogi, S. Kurita, *Bull. Chem. Soc. Jpn.* 55 (1982) 2254.
- [11] M. Hino, K. Arata, *J. Chem. Soc. Chem. Commun.* 18 (1988) 1259.
- [12] J.G. Santiesteban, J.C. Vartuli, S. Han, R.D. Bastian, C.D. Chang, *J. Catal.* 168 (1997) 431.
- [13] M. Hino, K. Arata, *Chem. Lett.* 6 (1989) 971.
- [14] C. Martin, G. Solana, P. Malet, V. Rives, *Catal. Today* 78 (2003) 365.
- [15] D.S. Kim, M. Ostromecki, I.E. Wachs, *J. Mol. Catal. A Chem.* 106 (1996) 93.
- [16] J.-M. Jehng, A.M. Turek, I.E. Wachs, *Appl. Catal. A* 83 (1992) 179.
- [17] I.E. Wachs, *Catal. Today* 27 (1996) 437.
- [18] R. Thomas, F.P.J.M. Kerkhof, J.A. Moulijn, J. Medema, V.H.J. de Beer, *J. Catal.* 61 (1980) 559.
- [19] P. Tiltarelli, A. Iannibello, P. Villa, *J. Solid State Chem.* 37 (1981) 95.
- [20] S.S. Chan, I.E. Wachs, L.L. Murrell, L. Wang, W.K. Hall, *J. Phys. Chem.* 88 (1984) 5831.
- [21] L. Salvati, L.E. Makovsky, J.M. Stencel, F.R. Brown, D.M. Hercules, *J. Phys. Chem.* 85 (1981) 3700.
- [22] P. Biloen, G. Pott, *J. Catal.* 30 (1973) 169.
- [23] S. Djerad, L. Tifouti, M. Crocoll, W. Weisweiler, *J. Mol. Catal. A Chem.* 208 (2004) 257.
- [24] J.A. Horsley, I.E. Wachs, J.M. Brown, G.H. Via, F.D. Hardcastle, *J. Phys. Chem.* 91 (1987) 4014.
- [25] M.M. Ostromecki, L.J. Burcham, I.E. Wachs, *J. Mol. Catal. A Chem.* 132 (1998) 59.
- [26] L.H. Gielgens, M.G.H. Vankampen, M.M. Broek, R. Vanhardeveld, V. Ponc, *J. Catal.* 154 (1995) 201.
- [27] J. Macht, C.D. Baertsch, M.M. Lozano, S.L. Soled, Y. Wang, E. Iglesia, *J. Catal.* 227 (2004) 479.
- [28] T. Feng, J.M. Vohs, *J. Catal.* 208 (2002) 301.
- [29] L.E. Briand, W.E. Farneth, I.E. Wachs, *Catal. Today* 62 (2000) 219.
- [30] P.A. Redhead, *Vacuum* 12 (1962) 213.
- [31] E.I. Ross, T.J. Kim, I.E. Wachs, in preparation.
- [32] L.A. Nafie, in: I.R. Lewis, H.G.M. Edwards (Eds.), *Handbook of Raman Spectroscopy*, Dekker, New York, 2001, p. 1.
- [33] M.A. Vuurman, I.E. Wachs, *J. Phys. Chem.* 96 (1992) 5008.
- [34] S.S. Chan, I.E. Wachs, L.L. Murrell, *J. Catal.* 90 (1984) 150.
- [35] W.V. Knowles, Ph.D. dissertation, Rice University, Houston, TX (2006).
- [36] M. Scheithauer, R.K. Grasselli, H. Knozinger, *Langmuir* 14 (1998) 3019.
- [37] Y.S. Chen, I.E. Wachs, *J. Catal.* 217 (2003) 468.
- [38] M. Scheithauer, T.K. Cheung, R.E. Jentoft, R.K. Grasselli, B.C. Gates, H. Knozinger, *J. Catal.* 180 (1998) 1.
- [39] C.D. Baertsch, S.L. Soled, E. Iglesia, *J. Phys. Chem. B* 105 (2001) 1320.
- [40] D.G. Barton, M. Shtein, R.D. Wilson, S.L. Soled, E. Iglesia, *J. Phys. Chem. B* 103 (1999) 630.
- [41] N. Vaidyanathan, M. Houalla, D.M. Hercules, *Catal. Lett.* 43 (1997) 209.
- [42] N. Vaidyanathan, D.M. Hercules, M. Houalla, *Anal. Bioanal. Chem.* 373 (2002) 547.
- [43] N. Vaidyanathan, M. Houalla, D.M. Hercules, *Surf. Interface Anal.* 26 (1998) 415.
- [44] C. Pfaff, M.J. Perez-Zurita, C. Scott, P. Patino, M.R. Goldwasser, J. Goldwasser, F.M. Mulcahy, M. Houalla, D.M. Hercules, *Catal. Lett.* 49 (1997) 13.
- [45] N. Naito, N. Katada, M. Niwa, *J. Phys. Chem. B* 103 (1999) 7206.
- [46] X.F. Yu, N.Z. Wu, H.Z. Huang, Y.C. Xie, Y.Q. Tang, *J. Mater. Chem.* 11 (2001) 3337.
- [47] J. Engweiler, J. Harf, A. Baiker, *J. Catal.* 159 (1996) 256.
- [48] G. Bond, S. Flamerz, L. van Wijk, *Catal. Today* 1 (1987) 229.
- [49] S.S. Chan, I.E. Wachs, L.L. Murrell, N.C. Dispenziere Jr., *J. Catal.* 92 (1985) 1.
- [50] L. Salvati, J.M. Makovsky, J.M. Stencel, F.R. Brown, D.M. Hercules, *J. Phys. Chem.* 85 (1981) 3700.
- [51] R.T. Sanderson, *J. Chem. Educ.* 65 (1988) 112.